Check for updates

ENGINEERING

Digital composites with reprogrammable phase architectures

Yun Bai[1]†, Xuebo Yuan[2]†, Yang Weng[1], Kaiping Yin[1], Heling Wang[3,4]*, Xiaoyue Ni[1,5]*

Copyright © 2026 The Authors, some rights reserved; exclusive licensee American Association for the Advancement of Science. No claim to original U.S. Government Works. Distributed under a Creative Commons Attribution NonCommercial License 4.0 (CC BY-NC).

Spatial patterning of material phases underpins the functional diversity of natural and engineered composites. However, phase architectures are typically fixed once formed, limiting adaptability. Here, we introduce a digital composite with reprogrammable solid-liquid phase architectures at voxel resolution. Each elastomeric voxel contains a liquid metal composite capable of electrically switching between nonvolatile solid and liquid states within seconds, analogous to rewriting data on a hard disk. High-throughput experiments and coupled modeling demonstrate precise tuning of viscoelastic and plastic properties, as well as programmable constitutive behaviors and strain distributions. A modular assembly strategy allows scalable 3D construction of reprogrammable composites into free-form, bulk geometries. By encoding phase states as digital inputs, the composite unlocks unprecedented access to real-time, voxel-level tuning of material properties.

INTRODUCTION

Materials prevalently comprise regions with contrasting properties—known as phases—that differ in composition, structure, or physical state. The spatial arrangement of these phases, or phase architecture, plays a central role in dictating a material's functional behavior (Fig. 1A). In natural materials, phase architectures usually exhibit complex, irregular topologies that give rise to emergent properties unattainable by their individual constituents, often enabling superior mechanical performance (*1*, *2*). Examples include vein-like networks in trabecular bone that resist fatigue (*3*), porous cellular structures in sea sponge that enhance energy absorption (*4*), and the brick-and-mortar architectures in nacre that improve fracture toughness (*5*).

Understanding and controlling phase architectures has long been a defining driver of materials science. It has evolved from thermodynamic microstructural tuning in metallurgy (*6*, *7*), to deterministic multimaterial patterning in composites, and now to voxel-level additive manufacturing (*8*–*10*) that enables programmable, complex architectures for precise tunability and unconventional properties (*11*–*16*). Despite these advances, phase architectures remain fixed once formed, locking materials into static and limited functionalities. Expanding the design space into the time domain is essential for adapting properties to meet evolving functional demands or mitigate trade-offs among competing performance requirements (*17*–*20*). Although various postfabrication reconfiguration strategies have emerged, they rely predominantly on geometric deformation to alter effective responses (*21*–*32*). A subset of these approaches can modulate local stiffness or damping with modest shape change, but they have yet to achieve voxel-addressable, nonvolatile control in a 3D continuum (*21*–*25*). As a result, these approaches inherently limit reprogrammability to one-dimensional (1D) or 2D elastic behaviors, falling short of supporting multidirectional tunability required for bulk material applications. Direct, on-demand programming of material phase architectures with stable memory in the deployment environment remains unrealized. Here, we introduce a digitally reprogrammable composite that achieves in situ, reversible control of solid-liquid voxels, enabling dynamic, user-defined phase patterning (Fig. 1A).

RESULTS

A solid-liquid composite with digitally reprogrammable phase architectures

As illustrated in Fig. 1B, the composite takes the form of a voxelated array of gold (Au)–coated polydimethylsiloxane (PDMS; Young's modulus, ~1 MPa) chambers, filled with liquid metal composite (LMC; Young's modulus, ~9 GPa) inclusions (figs. S1 and S2 and note S1 and see Materials and Methods). The LMC, composed of gallium (Ga; 95.2 wt %) and iron particles (Fe; 4.8 wt %), exhibits stable liquid and solid phases within the Au-coated PDMS chamber between a freezing point $T_f = 0.0$°C and a melting point $T_m = 29.0$°C. This thermal hysteresis arises from engineered supercooling. It defines the operating temperature range and is tunable by adjusting the iron content and the chamber-surface chemistry. The resulting window targets an optimum: large enough to retain either phase at room temperature yet small enough to permit rapid, energy-efficient phase transitions (fig. S3 and note S2 and see Materials and Methods). The sharp mechanical contrast between the solid and liquid states of each voxel, e.g., a sevenfold difference in an effective modulus at an LMC volume fraction of 0.43, gives rise to spatially heterogeneous phase architectures that underpin mechanical programmability (figs. S4 to S7 and notes S3 to S6). A flexible and stretchable array of electrodes, bonded to the top surface of the chambers, serves as a resistive network for voxel-resolved Joule heating and temperature sensing (Fig. 1C, figs. S8 to S11 and note S1 and see Materials and Methods).

Figure 1D shows voxel-level compliance measurement of a 3 × 3 sample during programming into a checkerboard configuration, followed by a locking process (fig. S12 and note S7 and see Materials and Methods). The programming process occurs at a controlled ambient temperature ($T_a = -10$°C, easily achievable through a semiconductor cooler) below T_f, where the solid phase of LMC is stable. When programming starts, embedded electrodes initiate localized thermal regulation to trigger and maintain the liquid state exclusively

[1]Department of Mechanical Engineering and Materials Science, Duke University, Durham, NC 27708, USA. [2]School of Mechanics and Aerospace Engineering, Southwest Jiaotong University, Chengdu 610031, China. [3]State Key Laboratory of Flexible Electronics Technology, Tsinghua University, Beijing 100084, China. [4]Institute of Flexible Electronics Technology of THU, Tsinghua University, Jiaxing 314000, China. [5]Department of Biostatistics and Bioinformatics, Duke University, Durham, NC 27708, USA.
*Corresponding author. Email: wanghl2006@tsinghua.edu.cn (H.W.); xiaoyue.ni@duke.edu (X.N.)
†These authors contributed equally to this work.

Downloaded from https://www.science.org on January 23, 2026

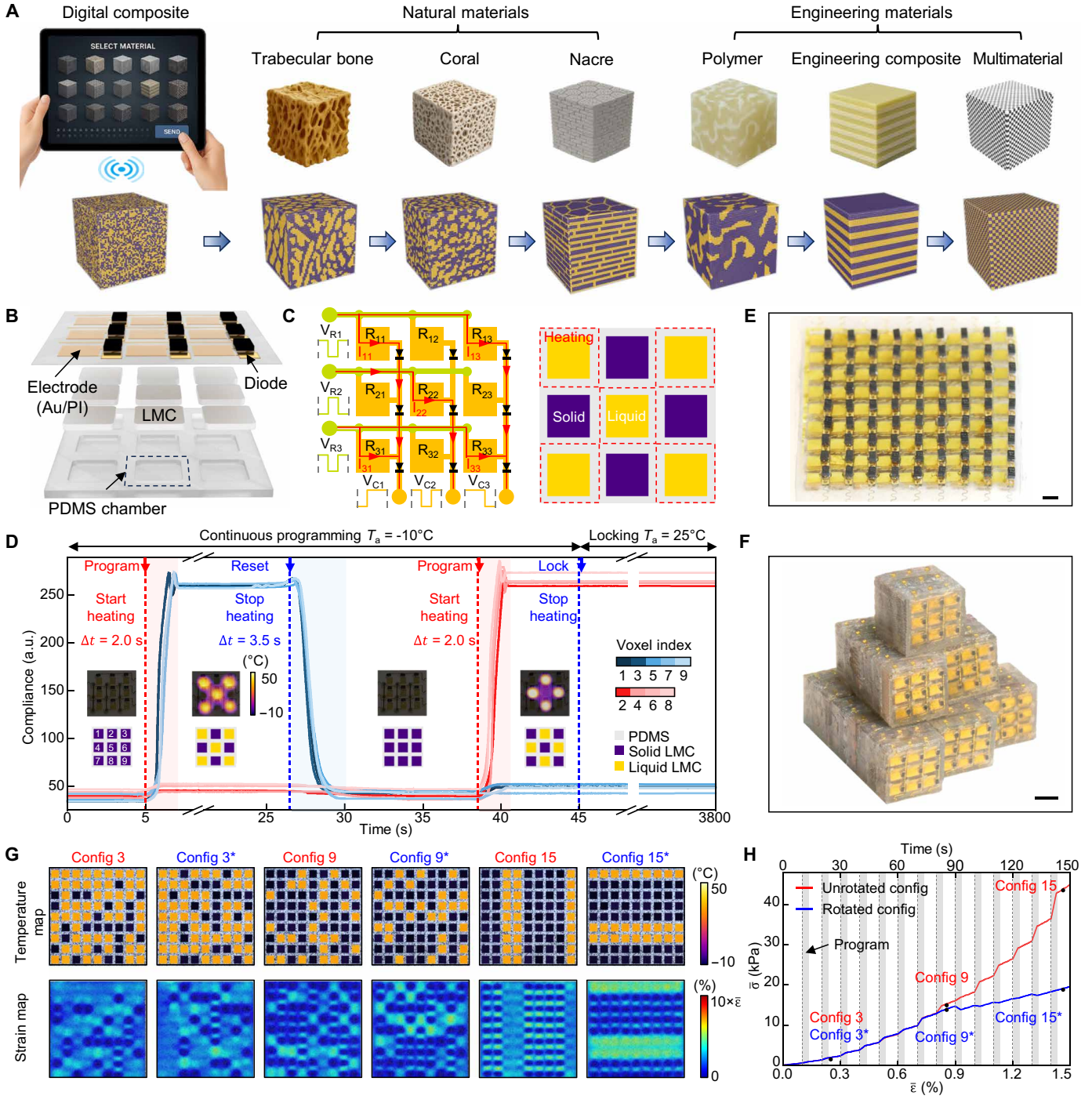

Fig. 1. Programming and testing of digital composite with nonvolatile solid-liquid phase architectures. (**A**) Concept of a digital composite with reprogrammable phase architectures, structurally inspired by micro- and mesostructures found in trabecular bone, sea sponge, nacre, polymer, engineering composite, and multimaterial. (**B**) Schematic illustration of a 2D digital composite with 3 × 3 voxel array, consisting of PDMS chambers (2.10 mm by 2.10 mm by 0.30 mm) filled with LMC (1.50 mm by 1.50 mm by 0.25 mm), and integrated flexible electrodes (1.25 mm by 1.25 mm) paired with surface-mounted diodes. (**C**) Schematic of the multiplexed circuit with row and column voltage inputs enabling voxel-resolved thermal control of solid-liquid phase transitions. (**D**) Continuous monitoring of surface compliance of each voxel in a 3 × 3 sample during programming and locking. (**E** and **F**) Optical images of a 2D 9 × 9 sample (E) and a 3D free-form, irregular bulk assembly (270 voxels, all programmable) (F). (**G** and **H**) Experimental results from quasi-static tensile tests on a 9 × 9 sample ($\dot{\bar{\varepsilon}} = 0.01\%\ s^{-1}$), sequentially programmed into 15 configurations, followed by a second test using their digital rotations. The shaded region indicates the programming window. The results include temperature and strain maps (G) and engineering stress-strain measurements (H), all synchronized in time. Scale bars, 2 mm. a.u., arbitrary units.

Downloaded from https://www.science.org on January 23, 2026

in target voxels while remaining functional for ≥500 stretch cycles at strains up to 13.6% (figs. S13 to S18 and notes S4 and S8 and see Materials and Methods). Pulsed heating with closed-loop temperature feedback enables rapid and stable melting while minimizing thermal cross-talk, achieving target voxel softening within 2.0 s under 0.2-W heating (0.7 J/mm^3). Ceasing heating allows them to solidify, rehardening within 3.5 s. From statistics over 100 heating-cooling cycles, the minimum reprogramming time is 3.02 ± 0.44 s, governed by the longer solidification process (figs. S12D and S20). Restoring T_a to room temperature (25°C) stabilizes the configuration without sustained heating. The locked configuration remains stable for an extended duration (>1 hour) under continuous indentation testing. This erase-write-store cycle functions analogously to a hard disk: The programmed material operates untethered during deployment and reconnects to a cooling socket only for reprogramming. The fast, nonvolatile phase-toggling mechanism underpins scalability, as it requires no energy to maintain the phase architecture. Such scalable design and control strategy enables the fabrication and integration of larger 2D and stacked 3D reprogrammable samples, as exemplified by the 9 × 9 array and a free-form, irregular bulk structure shown in Fig. 1 (E and F) (fig. S9 and see Materials and Methods).

The fast reprogrammability enables in situ experimentation using a custom platform for automated mechanical testing of 2D samples across varying phase architectures (figs. S21 to S24 and note S9 and see Materials and Methods). Figure 1 (G and H) presents the testing results of a 9 × 9 sample under a constant strain rate of 0.01% s^{-1}, sequentially programmed into 15 configurations (figs. S25 and S26, movie S1, and note S10). Digitally rotating the phase architectures, as illustrated by the temperature and the maximum principal strain (ε_1) maps (Fig. 1G), enables biaxial (x and y axes) measurements using uniaxial (x axis) testing. The engineering stress-strain ($\bar{\sigma} - \bar{\varepsilon}$) curves reveal the evolution of mechanical responses over configurations, with anisotropy developing from configuration 9 onward (Fig. 1H).

Reprogrammable viscoelasticity

Voxel-level control of phase architectures allows the composite to exhibit diverse, time-varying mechanical behaviors. An inverse design approach, enabled by a simplified finite-element (FE) model validated by full finite-element analysis (FEA), interrogates the design space (figs. S27 to S29 and notes S4, S11, and S12). This framework reveals independently programmable viscoelastic parameters, including the complete set of linear elastic constants—Young's modulus (E_x and E_y), Poisson's ratio (ν_{xy} and ν_{yx}), shear modulus (G_{xy})—and loss factors ($\tan\delta_x$ and $\tan\delta_y$ at 1 Hz) for 2D systems under uniaxial tension (figs. S30 and S31).

The automated experimental platform programs each 2D pattern in a 9 × 9 sample and outputs effective viscoelastic properties ($\bar{E}_x$, $\bar{\nu}_{xy}$, and $\tan\bar{\delta}_x$) in 8.7 s (figs. S32 and S33 and notes S10 and S13). This throughput supports biaxial characterization of 60,475 configurations within a week. A hybrid sampling strategy, combining random sampling, genetic algorithm, and inverse design, generates these configurations to densely populate and span the theoretically bounded tensile modulus space (fig. S34 and notes S14 and S15). Of these, 10,115 of which are nearly isotropic (see Materials and Methods). Figure 2A reports means from 20 independent tests per configuration, with each test performed after completing a full reprogramming cycle. The results demonstrate a broad range of reprogrammability, high reproducibility (fig. S35), and close agreement with FEA predictions (Fig. 2B).

The high-throughput testing enables a detailed investigation of the relationship between topological features and mechanical properties. Increasing the solid voxel fraction (C_{solid}; fig. S36 and note S16) generally raises $\bar{E}_x$ while reducing $\bar{\nu}_{xy}$ and $\tan\bar{\delta}_x$, with stronger correlations observed in isotropic configurations (Fig. 2C). At fixed C_{solid}, increasing average chain length along the loading direction ($\bar{L}_x$; fig. S36 and note S16) yields linear trends, highlighting the role of solid-voxel interconnectivity (Fig. 2D). Among various topological parameters related to disorder, heterogeneity, and anisotropy, $\bar{L}_x$ exhibits the strongest correlation with viscoelastic properties (figs. S37 and S38 and note S16). Testing on 3D-printed multimaterials supports the generality of the observed topological feature-property relationships (fig. S39 and note S17).

Figure 2E shows a 3D Ashby plot of the studied viscoelastic properties, illustrating the fine tunability achieved by the 9 × 9 sample within the design space (fig. S40). Defining the normalized distance from a point as $\Delta r = \sqrt{\left(\Delta\bar{E}_x/\bar{E}_x\right)^2 + \left(\Delta\bar{\nu}_{xy}/\bar{\nu}_{xy}\right)^2 + \left(\Delta\tan\bar{\delta}_x/\tan\bar{\delta}_x\right)^2}$, the average nearest-neighbor distance, $\tilde{\Delta}r$, is on the order of 10^{-2} across the tested configurations. The inverse design predicts a decrease in $\tilde{\Delta}r$ with larger system size (fig. S41). A global search within the nearly isotropic property space efficiently identifies configurations whose effective viscoelastic properties closely mimic those of a range of existing materials, with $\Delta r < 10^{-2}$ (Fig. 2E, fig. S42, and movie S2).

Reprogrammable plasticity

Beyond the small deformation regime, irreversible deformation occurs. Figure 3A shows the $\bar{\sigma} - \bar{\varepsilon}$ data obtained from two representative configurations of a 9 × 9 sample, both with $C_{solid} = 0.49$, strained to a maximum of 6% at a rate of 1% s^{-1}. The tensile test tracks the onset of abrupt deviation from the initial linear loading curve to identify the elastic limit, i.e., the yield strain ($\bar{\varepsilon}_Y$; figs. S43 and S44 and note S10). A distinctive feature of the digital composite is its reversible plasticity, achieved through the reset process—melting all voxels—which allows it to return to its original configuration even after undergoing conventional "irreversible" deformation. This behavior is confirmed through 100 repetitive loading cycles, with all $\bar{\sigma} - \bar{\varepsilon}$ curves and corresponding strain maps closely replicating the initial cycle.

The ability to repeat plasticity tests on the same sample enables investigation of yielding mechanisms that are robust to defects and sample-to-sample variability. The automated experiment performs 20-cycle plasticity tests across the same 60,475 configurations examined in Fig. 2 and identifies the average $\bar{\varepsilon}_Y$ for each, excluding the all-liquid one (fig. S45). In situ imaging of representative configurations reveals that yielding originates from interfacial delamination between solid LMC and PDMS matrix (Fig. 3B, fig. S46, and note S18). Notably, initial delamination does not always occur at the solid voxel experiencing the maximum ε_1 (Fig. 3B). This observation motivates the development of a model based on energy minimization to predict the onset of delamination (section S18) (*33*). Using the interfacial adhesion energy measured via a standard pullout test ($\gamma_a = 0.324$ J/m^2; fig. S47 and note S18), the model predicts $\bar{\varepsilon}_Y$ with a mean relative error of 85.9% and an SD of 47.5% compared to experimental measurements (Fig. 3C). Incorporating voxel-specific calibration of γ_a improves model accuracy, reducing the mean relative error to 4.6% and the SD to 25.9% (figs. S48 and S49 and note

Downloaded from https://www.science.org on January 23, 2026

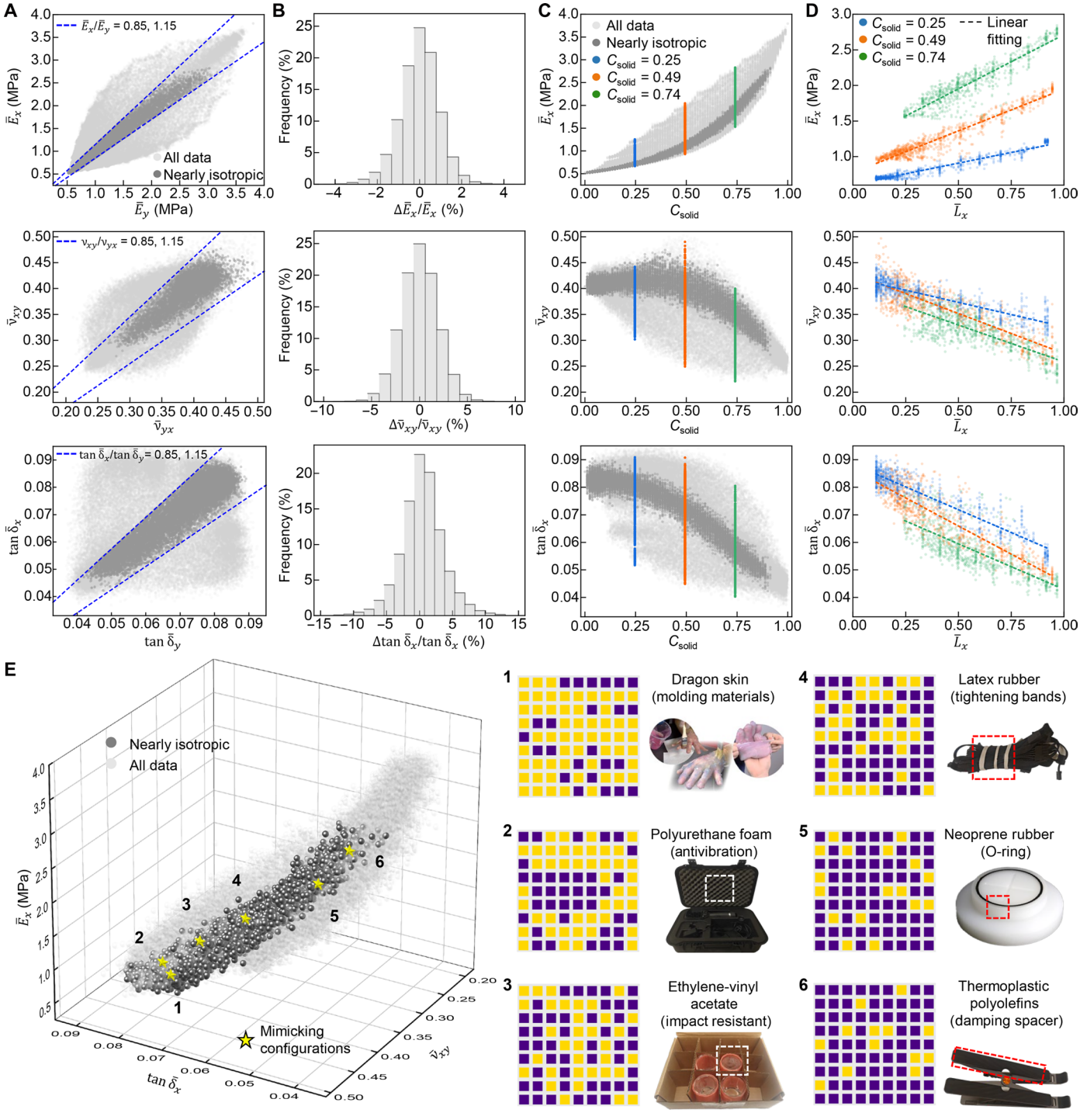

Fig. 2. High-throughput mapping of reprogrammable viscoelastic properties with multiparametric and multidirectional resolution. (**A**) Experimental characterization of effective Young's modulus ($\bar{E}$), Poisson's ratio ($\bar{\nu}$), and loss factor ($\tan\bar{\delta}$) in both column (x) and row (y) directions of a 9 × 9 digital composite across 60,475 configurations. Among them, 10,115 configurations are nearly isotropic. Each data point represents the mean of 20 tests. (**B**) Histograms showing the relative differences between experimental results and FEA predictions for $\bar{E}_x$, $\bar{\nu}_{xy}$, and $\tan\bar{\delta}_x$, with maximum absolute deviations of 4.3, 8.5, and 14.6%, respectively. (**C**) Effective viscoelastic properties versus solid voxel fraction (C_{solid}). (**D**) Effective viscoelastic properties versus average chain length along the loading direction ($\bar{L}_x$; normalized by system size $N = 9$) at fixed C_{solid}. (**E**) 3D Ashby plot of effective viscoelastic properties across all configurations. Nearly isotropic configurations are identified to emulate the viscoelastic behaviors of six different commercially available materials.

Downloaded from https://www.science.org on January 23, 2026

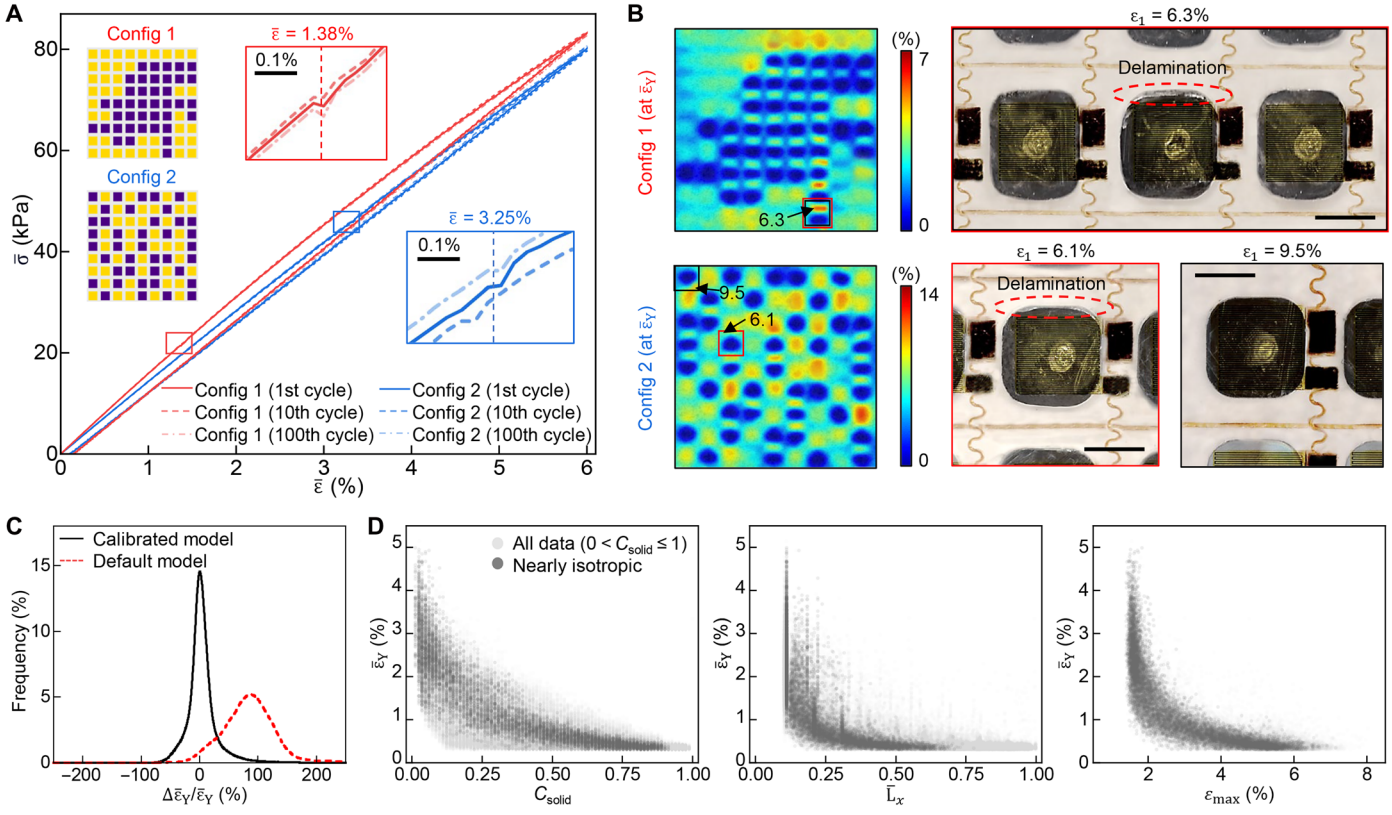

Fig. 3. High-throughput characterization of reprogrammable yielding behavior via repeatable plasticity testing. (**A**) Stress-strain responses over 100-cycle tensile tests on a 9 × 9 sample with two configurations at C_{solid} = 0.49 reveal repeatable yet configuration-dependent yielding behavior ($\bar{\varepsilon}_Y$ = 1.38 ± 0.10% and 3.25 ± 0.12%, respectively). Insets highlight the regions near the yield strain ($\bar{\varepsilon}_Y$), identified as the point of abrupt deviation from linear loading. (**B**) Representative strain maps of the two configurations at $\bar{\varepsilon}_Y$, with optical images zoomed in on the delaminated voxel (red box) and the solid voxel exhibiting the maximum ε_1 (black box). In configuration 1, delamination occurs at the voxel with the maximum ε_1; in configuration 2, it occurs at a different solid voxel despite a lower local strain. (**C**) Histogram of the discrepancy between experimentally measured and model-predicted $\bar{\varepsilon}_Y$ for all configurations evaluated in Fig. 2, excluding the all-liquid one. The default model uses a uniform interfacial adhesion energy (γ_a) measured from standard pullout test, while the calibrated model uses voxel-specific γ_a inversely calculated from experiments on single-solid-voxel configurations. (**D**) Experimentally measured $\bar{\varepsilon}_Y$ versus C_{solid}, $\bar{L}_x$, and ε_{max} (at $\bar{\varepsilon}$ = 1%). Each data point represents the mean of 20 tests. Scale bars, 1 mm.

S18). The high-throughput dataset suggests that $\bar{\varepsilon}_Y$ decreases with increasing C_{solid}, $\bar{L}_x$, and ε_{max} (maximum ε_1 at $\bar{\varepsilon}$ = 1%), indicating a potential relationship between plastic and viscoelastic parameters (Fig. 3D and fig. S50).

Reprogramming stress and strain responses

Beyond the overall effective properties, the rapid reconfiguration of phase architectures also enables the dynamic programming of detailed mechanical responses. Leveraging independently reprogrammable modulus and thermal stress, the material generates a range of target stress-strain responses by progressing through an inverse-designed sequence of phase architectures over 40 uniform strain steps (figs. S29 and S51 to S54 and notes S4 and S12). Figure 4 (A to D) demonstrates the programming of effective constitutive behaviors of a 9 × 9 sample, strained to a maximum of 1% at a rate of 0.005% s^{-1}, mimicking conventional and unconventional elastic, plastic, and viscoelastic responses, as well as complex, heart-shaped stress-strain curves (movie S3). The experimental results closely match the target, with a maximum stress deviation of 11.8%. Increasing the number of steps smooths the curve and improves proximity to the target (fig. S55).

The precise reprogramming of phase architectures also enables active mitigation of strain localization under varying loading conditions, potentially enhancing the composite's load-bearing capacity. Figure 4 (E to G) compares the strain distributions of the digital composite with a random configuration versus optimized ones (fig. S29 and note S12) under three loading conditions—pure tension, pure shear, and combined tension-shear. In all three cases, optimized configurations reduce ε_{max} by more than 20% relative to the random one while maintaining relatively unchanged elastic properties ($\overline{E}_x$ = 1.49 ± 0.02 MPa; $\overline{G}_{xy}$ = 0.50 ± 0.02 MPa) (figs. S56 and S57). The same optimization method can minimize ε_{max} in other scenarios, including those involving varying stiffness requirements, complex boundary conditions, or internal defects (figs. S57 to S59).

Reprogrammable 3D digital composite

Layers of 2D digital composites with cubic voxels can be stacked and bonded to form 3D arrays. Small 3D units serve as modular building blocks, enabling reprogramming and assembly into larger 3D structures with diverse forms and geometries, analogous to LEGO bricks. Figure 5 (A and B) shows an illustration and an optical image of a custom socket interface equipped with a cooling module for programming a 3 × 3 × 3 unit at T_a = −10.0°C (figs. S60 and S61 and note S19). Each reprogramming cycle takes ~25 s (fig. S62 and note S19). This interface-based design enables the creation of untethered,

Downloaded from https://www.science.org on January 23, 2026

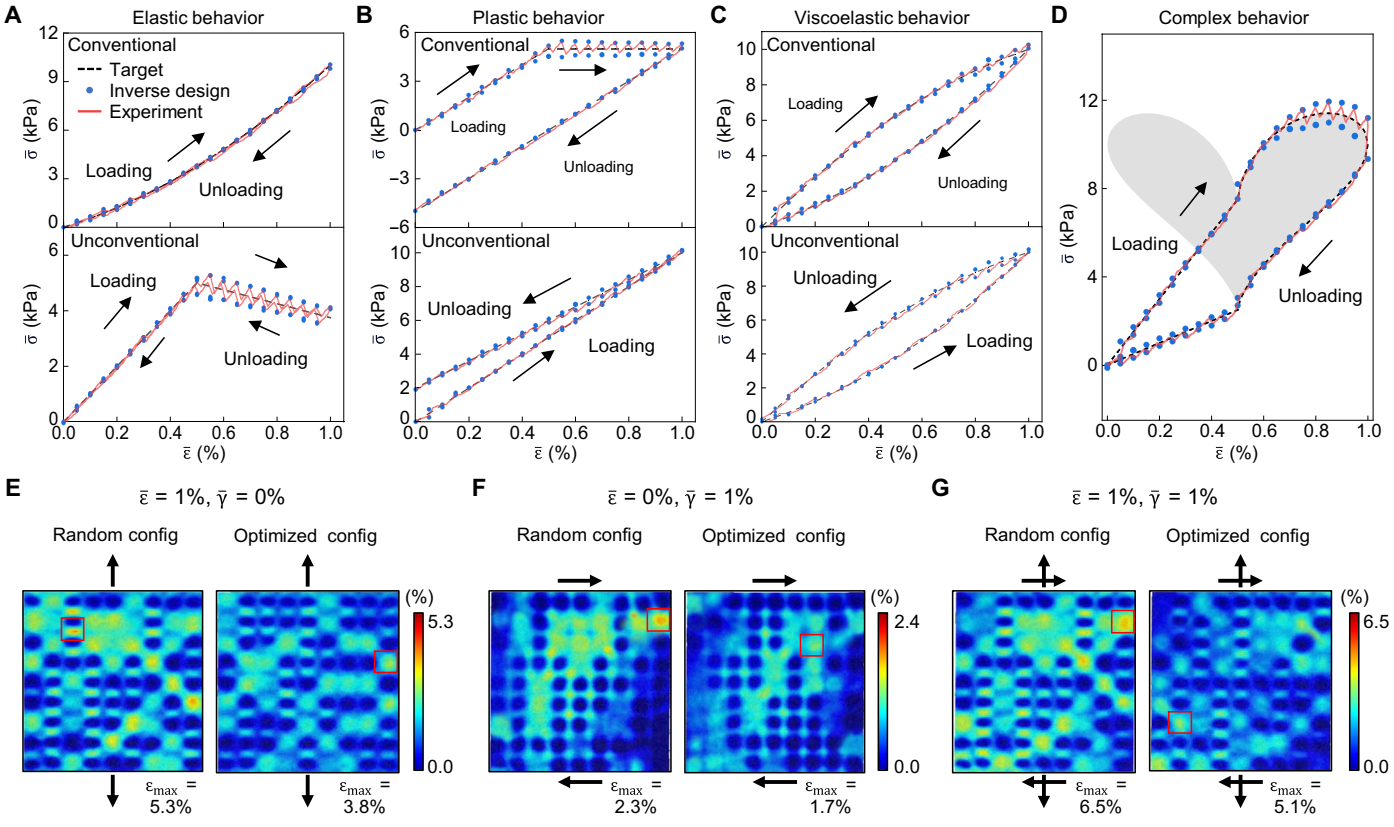

Fig. 4. Controlling global stress-strain responses and local strain distributions via dynamic programming of phase architectures. (**A** to **D**) A 9 × 9 sample, subjected to prescribed loading function ($\bar{\varepsilon}_{max} = 1\,\%, \dot{\bar{\varepsilon}} = 0.005\%\ s^{-1}$) and sequentially programmed into 40 inverse-designed phase architectures to produce a target effective stress-strain curve. The results include both conventional and unconventional elastic (A), plastic (B), viscoelastic (C), and complex behaviors (D). (**E** to **G**) Strain maps of a 9 × 9 sample with a random configuration compared to configurations optimized to minimize ε_{max} while keeping elastic moduli unchanged, under three loading conditions: pure stretching (E), pure shearing (F), and combined stretching and shearing (G). The optimization shifts the locations of ε_{max} (red boxes) and reduces its magnitude by 27, 29, and 21%, respectively.

stand-alone 3D units with reprogrammable mechanics (fig. S63, movie S4, and note S19). Applying a thin layer of modified PDMS film (150 μm) as a reversible adhesive (*34*) allows robust assembly of multiple units into larger bulk (Fig. 5C). The interface reaches ~30-kPa strength with 100% reversible assembly yield. Disassembly via isopropyl alcohol (IPA) infiltration does not compromise the structural integrity or functionality of individual units—even after 100 reassembly cycles (fig. S64, movie S5, and note S20).

Figure 5D shows a 6 × 6 × 6 cube, assembled from eight units, under uniaxial compression. Leveraging 3D reprogrammability, the test outputs $\bar{E}_x$, $\bar{\nu}_{xy}$, $\bar{\nu}_{xz}$, and $\tan\bar{\delta}_x$ for 37 configurations, showing close agreement with FEA predictions (Fig. 5E). Similar to 2D systems, increasing C_{solid} tends to raise $\bar{E}_x$ and decrease $\tan\bar{\delta}_x$, $\bar{\nu}_{xy}$, and $\bar{\nu}_{xz}$ (Fig. 2C and fig. S65). Extending the simplified FE model to 3D enables inverse design of large cube samples with target elastic behaviors and supports investigation of topological features-property relationships analogous to those in 2D (figs. S29 and S66 to S69 and note S12).

Figure 5F presents a 3 × 3 × 30 beam, composed of 10 units, functioning as a reprogrammable tail appendage for a robotic fish to passively control its swimming motion. Three distinct configurations, each with $C_{solid} \approx 0.1$, are subjected to a flexural vibration test with a 0.5-mm driving amplitude for mechanical characterization (Fig. 5G, fig. S70, movie S6, and note S21), followed by a swimming test under fixed electromagnetic coil actuation (Fig. 5H, fig. S71, movie S7, and note S22). Configuration 1, with all solid voxels positioned far from the actuation point, exhibits symmetric flexural motion, allowing efficient straight-line swimming. Configuration 2, with all solid voxels eccentrically aligned, exhibits asymmetric vibration with 80% less displacement on the solid-concentrated side, resulting in a turning motion and a spiral path. Configuration 3, with a helical arrangement of solid voxels, induces torsional motion under pure flexural vibration. This energy transfer into nonpropulsive torsion markedly reduces the forward displacement, leaving no observable movement over 600 s.

DISCUSSION

This work presents a transformative strategy for achieving rapid, digital, and nonvolatile control of millimeter-scale, voxelated phase architectures in a solid-liquid composite, enabled by a hard disk–like erase-write-store cycle through engineered supercooling windows. The platform technology lays the foundation for unprecedented phase-level reprogrammability and is readily extendable beyond the studied PDMS-LMC system—for example, using phase-change materials with tailored thermal hysteresis to suit different working

Downloaded from https://www.science.org on January 23, 2026

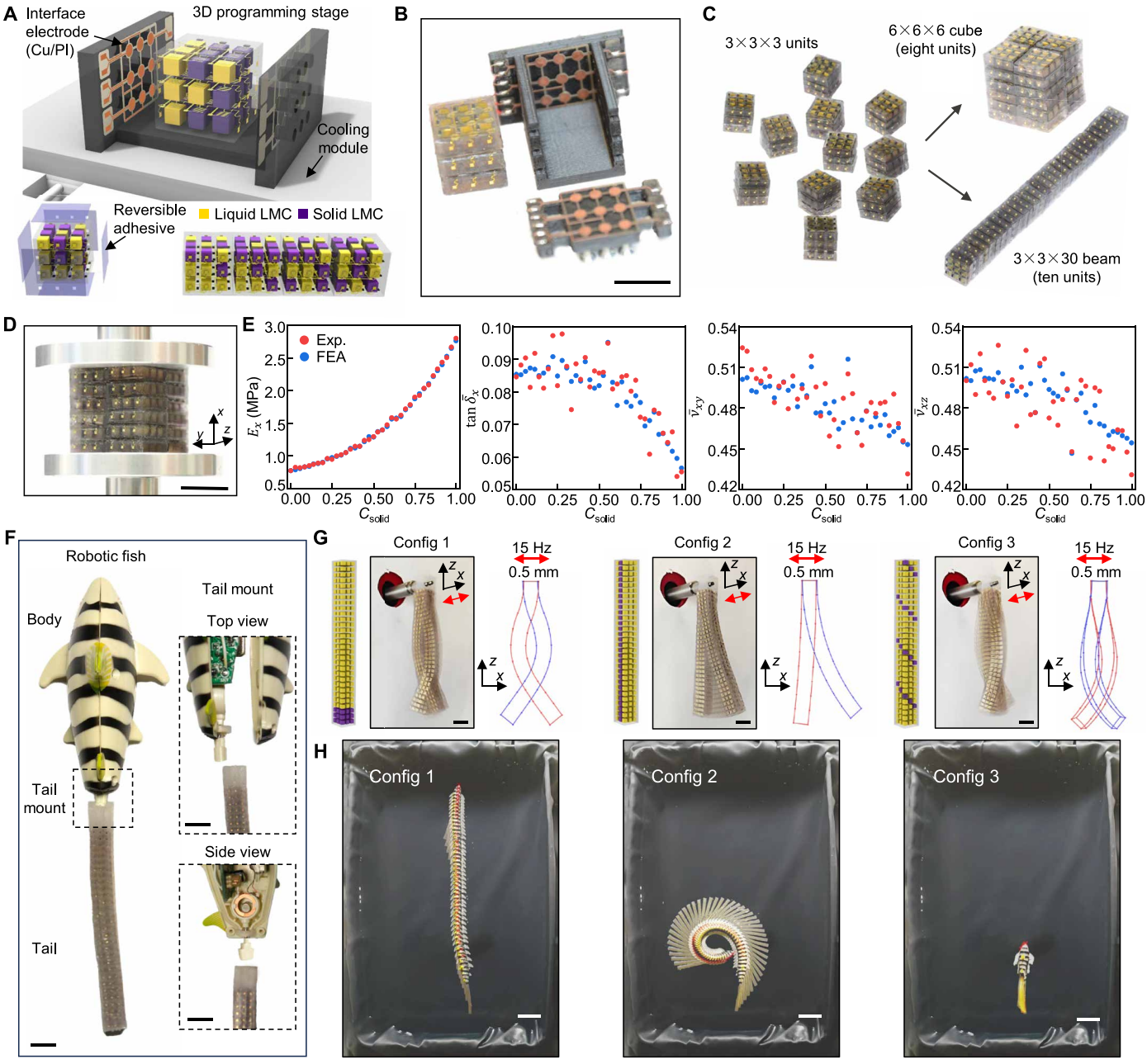

Fig. 5. Programming 3D digital composite. (**A**) Schematic of the 3D programming and assembly process. A custom socket interface delivers programming signals to a 3 × 3 × 3 unit. Reversible adhesives enable modular, reconfigurable assembly of 3D units into large-scale structures. (**B**) Optical image of the 3D programming stage and a 3D unit with cubic voxels (3.50 mm by 3.50 mm by 3.50 mm). Scale bar, 10 mm. (**C**) Optical images of modular 3D units assembled into reconfigurable 3D structures, including a 6 × 6 × 6 cube (8 units) and a 3 × 3 × 30 beam (10 units). (**D**) Optical image of a 6 × 6 × 6 cube under uniaxial compression (*x* axis). Scale bar, 10 mm. (**E**) Experimental and FEA results of $\bar{E}_x$, tan$\bar{\delta}_x$, $\bar{\nu}_{xy}$, and $\bar{\nu}_{xz}$ versus C_{solid} across 37 configurations of the 6 × 6 × 6 cube, showing maximum absolute deviations of 4.5, 6.7, 5.9, and 10.5%, respectively. (**F**) Optical image of a robotic fish with a 3 × 3 × 30 beam functioning as a reprogrammable tail appendage. Insets show top and side views of the disassembled tail mount. Scale bars, 10 mm. (**G**) A 3D beam with three distinct configurations and similar C_{solid} (≈ 0.1) undergoing flexural vibration at 15 Hz with 0.5-mm peak-to-peak driving amplitude along the *x* axis. Each panel shows a configuration schematic, a composite optical image, and a 3D reconstruction of the beam at maximum steady-state deflections. Scale bars, 10 mm. (**H**) Composite time-lapse images of a robotic fish with a 3D beam tail appendage in the same three configurations, swimming in a water tank under identical actuation conditions (15-Hz flexural vibration via built-in magnetic coils). Red crosses mark the fish head positions at 1-s intervals. Scale bars, 10 cm.

Downloaded from https://www.science.org on January 23, 2026

temperatures. Future efforts will focus on decoupling reprogrammability from an ambient cooling environment by integrating active cooling strategies (*35*, *36*). Alternatively, for applications where power consumption and physical tethering are not limiting factors, using materials that solidify above the operational temperature offers a simpler route for in situ programming without the need for cooling. Although the present implementation is laboratory scale, the voxel architecture and digital addressing circuits are fundamentally compatible with batch molding, high-throughput microfabrication, and modular assembly. Further study may explore advanced manufacturing techniques (e.g., 3D printing) for scaling, homogenization, and hierarchical structuring of the composite to support larger and more complex systems. For miniaturization, future studies should assess size effects and fabrication feasibility as voxel dimensions reduce (*37*, *38*).

Unlike one-time-fabricated materials, the digital composite establishes a high-throughput and resource-efficient platform for data-driven exploration of heterogeneous mechanics, where integration with artificial intelligence can further accelerate inverse design for nontrivial mechanical behaviors, harnessing the untapped potential of complex phase topology (*39*, *40*). With stable memory, the system is practical in generating real-world data, particularly valuable for investigating 3D mechanical behaviors involving nonlinearity and irreversibility under actual deployment conditions. Specifically, the reversible plastic deformation makes it possible to design and make use of yielding behavior for efficient, robust energy dissipation.

Toward multifunctionality, integrating smart materials or structures with the composite could enable simultaneous control of force actuation and mechanical properties, unlocking new classes of unconventional mechanical machines (*41*, *42*). Incorporating sensing elements could provide closed-loop feedback and adaptive control, endowing the reprogrammable materials with autonomy and embedded intelligence capable of dynamically co-optimizing both structural configuration and material response (*43*–*45*). The demonstrated digital control of phase states could be extended to other functional domains, such as optics (*46*, *47*) and magnetics (*48*, *49*). The platform establishes a paradigm of reconfigurable materials, creating opportunities for soft robotics, adaptive structures, autonomous systems, and beyond.

MATERIALS AND METHODS

Fabrication of the voxel array

The molds for the silicone chambers were fabricated using a stereolithography printer (FormLabs Form 3+) with high-temperature resin. The surfaces of the molds were coated with polyethylenimine (Sigma-Aldrich, 80% ethoxylated) solution for demolding. The PDMS (SYLGARD 184, DOW), with a base-to-cure agent ratio of 10:1, was molded and cured in an oven at 80°C for 2 hours. A hole (0.35 mm in diameter) was manually punched in the substrate of each chamber for vacuum filling. The capping layer was prepared by spin-coating PDMS onto a silicon wafer with a poly(methyl methacrylate) (PMMA) sacrificial layer. A thin layer of Au was selectively deposited on the inner surfaces of the chamber using a laser-cut mask. Plasma treatment was used to bond the undercut capping layer to the open chamber, completing the encapsulation. The LMC was prepared by melting 10 g of pure Ga (Sigma-Aldrich, 99.999%) in a glass beaker at 60°C with the addition of 0.5 g of Fe microparticles (Sigma-Aldrich, 10 μm in diameter). A 100-ml volume of a 3 M hydrochloric acid (HCl, Sigma-Aldrich) was added, and the mixture was stirred at 1000 rpm for 2 hours (L5M-A, Silverson). The mixture was separated from the liquid using a magnet and then rinsed with deionized water followed by IPA to remove any residual HCl. After applying a droplet of LMC (~0.5 mg) to each inlet, the sample was placed in a vacuum oven at 60°C and 0.5 mtorr for 5 min. Restoring atmospheric pressure drove LMC (3.3 ± 0.2 mg) into the chamber. After cleaning the residual LMC with IPA, each inlet was sealed with Sil-Poxy (Smooth-On).

Differential scanning calorimetry analysis

Differential scanning calorimetry (DSC; TA Instruments Q2 2500) was used to characterize the phase transitions of LMC within individual chambers. Single-chamber samples were prepared for DSC analysis. Each sample was equilibrated at 50°C, cooled to −80°C at a rate of −10°C/min, and then reheated to 50°C at a rate of 10°C/min. Results were averaged across three independent samples, each undergoing three complete thermal cycles.

Fabrication of the electrode array

The fabrication of the electrode array began with spin-coating a layer of polyimide (PI; PI2545, HD MicroSystems) onto a silicon wafer with PMMA (80 nm in thickness) as the sacrificial layer. The electron beam evaporation deposition process created a layer of titanium/gold (Ti/Au, 10 nm/100 nm). Photolithography and wet etching were performed to pattern the column- and row-addressing electrodes. A second PI layer (3.75 μm in thickness) was spin-coated to encapsulate the electrodes. Photolithography and reactive ion etching defined the outline of the encapsulated array and the Au-exposed regions for soldering and via connection. The sacrificial PMMA layer was undercut to transfer the electrodes from the silicon wafer to a water-soluble polyvinyl alcohol (PVA) tape. A layer of SiO_2 (100 nm in thickness) was deposited onto the arrays on the PVA tape. Plasma treatment enabled bonding of the row-addressing electrodes to a PDMS substrate (25 μm in thickness) on a glass side with a PMMA sacrificial layer. PVA tape was dissolved to expose Au. The column-addressing array was transferred from the PVA tape to a heat-release tape to expose Au. A layer of SiO_2 (100 nm in thickness) was selectively deposited on the PI-encapsulated regions of the column-addressing array, followed by plasma treatment to enable bonding to the PDMS substrate. The via holes were aligned and filled using silver epoxy. Heating to 80°C bonded the row-addressing array and removed the heat-release tape. Diodes were soldered onto the Au-exposed regions on the row-addressing array using silver epoxy.

Multiplexed circuit

The heating and sensing circuit used (i) I^2C-controlled pulse-width modulation (PWM) drivers (PCA9685), (ii) power amplifier circuits with metal–oxide–semiconductor field-effect transistors (MOSFETs; IRLZ44NPBF), (iii) a single-board computer (Raspberry Pi 5), (iv) an Intel NUC (Intel Core i7-8559U CPU, 2.70 GHz base frequency), and (v) two data acquisition (DAQ) modules (NI-9252, National Instruments). Programming signals were wirelessly transmitted from the NUC to the Raspberry Pi via Python socket communication. The Raspberry Pi issued control signals to the PWM drivers, which addressed the MOSFET gates for row-column electrode activation. Each MOSFET, powered by a 48-V dc supply (DP832A, RIGOL), modulated the multiplexer channel output at 100 Hz. Voltage drops across pull-up resistors were measured via the differential analog

Downloaded from https://www.science.org on January 23, 2026

inputs of the DAQ modules. Electrode resistance was computed using a voltage divider model.

Multilayer integration

For 2D sample integration, the electrode array was aligned and bonded to the corresponding LMC array with Sil-Poxy. The sample contour was defined by laser cutting, and the PMMA substrate was subsequently undercut to release the freestanding structure. For the 3D sample, the electrode array was folded to align with the LMC array and bonded with Sil-Poxy to form a single-layer stack. Using 3D-printed molds, a 4-mm-thick encapsulating layer was created. Multiple layers were stacked and bonded to form 3D structures using Sil-Poxy.

Indentation test

Custom magnetic coil-driven indenters were aligned and mounted onto the surface of the corresponding voxels. Each indenter was equipped with an integrated accelerometer (ADXL326BCPZ) to monitor the motion of the tip under fixed power input.

Mechanical test

The tensile test was performed by a custom multifunctional testing stage, which consists of a linear translation stage (LTS150C, Thorlabs) and a force gauge (M7-012, Mark-10) with a pair of tensile grips (G1008, Mark-10). Shear loading incorporates an additional translational stage in the orthogonal direction. The dynamic mechanical tensile test was conducted with a preload of 0.175% strain, a strain amplitude of 0.125%, and a frequency of 1 Hz for 5 s. The effective Young's modulus was estimated as the dynamic modulus amplitude. The compression test was conducted using the same testing stage with the grips replaced by compression plates (G1009-1, Mark-10). The dynamic mechanical compression test was conducted with a preload of 1.75% strain, a strain amplitude of 1.25% strain, and a frequency of 1 Hz for 5 s. The testing methods were validated against the standard testing results using the RSA-G2 Solids Analyzer (TA Instruments).

Optical imaging and digital image correlation

In situ optical imaging was performed by an optical camera (Canon EOS R) and a resolution of 3840 × 2160. For DIC, a speckle pattern was applied to one side of the sample by aerosol-spraying graphite using IPA as a carrier. DIC analysis used Ncorr, an open-source 2D DIC program in MATLAB, with a spatial resolution of 20 μm.

Identification of nearly isotropic configurations

Nearly isotropic configurations were identified as those where theoretical predictions (FEA) of E_x / E_y, ν_{xy} / ν_{yx}, $\tan\delta_x / \tan\delta_y$, and the Zener ratio $Z = 2(1+\nu_{xy})G_{xy} / E_x$ all fall between 0.85 and 1.15.

Supplementary Materials

The PDF file includes:
Supplementary Notes S1 to S22
Figs. S1 to S71
Table S1
Legends for movies S1 to S7
References

Other Supplementary Material for this manuscript includes the following:
Movies S1 to S7

REFERENCES

1. U. G. K. Wegst, H. Bai, E. Saiz, A. P. Tomsia, R. O. Ritchie, Bioinspired structural materials. *Nat. Mater.* **14**, 23–36 (2015).
2. M. Zaiser, S. Zapperi, Disordered mechanical metamaterials. *Nat. Rev. Phys.* **5**, 679–688 (2023).
3. A. M. Torres, A. A. Trikanad, C. A. Aubin, F. M. Lambers, M. Luna, C. M. Rimnac, P. Zavattieri, C. J. Hernandez, Bone-inspired microarchitectures achieve enhanced fatigue life. *Proc. Natl. Acad. Sci. U.S.A.* **116**, 24457–24462 (2019).
4. R. Zhao, E. Amstad, Bio-informed porous mineral-based composites. *Small* **21**, e2401052 (2025).
5. Z. Yin, F. Hannard, F. Barthelat, Impact-resistant nacre-like transparent materials. *Science* **364**, 1260–1263 (2019).
6. C. Liu, J. Lertthanasarn, M.-S. Pham, The origin of the boundary strengthening in polycrystal-inspired architected materials. *Nat. Commun.* **12**, 4600 (2021).
7. X. Li, L. Lu, J. Li, X. Zhang, H. Gao, Mechanical properties and deformation mechanisms of gradient nanostructured metals and alloys. *Nat. Rev. Mater.* **5**, 706–723 (2020).
8. M. A. Skylar-Scott, J. Mueller, C. W. Visser, J. A. Lewis, Voxelated soft matter via multimaterial multinozzle 3D printing. *Nature* **575**, 330–335 (2019).
9. X. Kuang, J. Wu, K. Chen, Z. Zhao, Z. Ding, F. Hu, D. Fang, H. J. Qi, Grayscale digital light processing 3D printing for highly functionally graded materials. *Sci. Adv.* **5**, eaav5790 (2019).
10. J. J. Martin, B. E. Fiore, R. M. Erb, Designing bioinspired composite reinforcement architectures via 3D magnetic printing. *Nat. Commun.* **6**, 8641 (2015).
11. N. Aage, E. Andreassen, B. S. Lazarov, O. Sigmund, Giga-voxel computational morphogenesis for structural design. *Nature* **550**, 84–86 (2017).
12. K. Liu, R. Sun, C. Daraio, Growth rules for irregular architected materials with programmable properties. *Science* **377**, 975–981 (2022).
13. D. R. Reid, N. Pashine, J. M. Wozniak, H. M. Jaeger, A. J. Liu, S. R. Nagel, J. J. de Pablo, Auxetic metamaterials from disordered networks. *Proc. Natl. Acad. Sci. U.S.A.* **115**, E1384–E1390 (2018).
14. H. Laubie, F. Radjai, R. Pellenq, F.-J. Ulm, Stress transmission and failure in disordered porous media. *Phys. Rev. Lett.* **119**, 075501 (2017).
15. G. Bordiga, E. Medina, S. Jafarzadeh, C. Bösch, R. P. Adams, V. Tournat, K. Bertoldi, Automated discovery of reprogrammable nonlinear dynamic metamaterials. *Nat. Mater.* **23**, 1486–1494 (2024).
16. B. Li, B. Deng, W. Shou, T.-H. Oh, Y. Hu, Y. Luo, L. Shi, W. Matusik, Computational discovery of microstructured composites with optimal stiffness-toughness trade-offs. *Sci. Adv.* **10**, eadk4284 (2024).
17. X. Xia, C. M. Spadaccini, J. R. Greer, Responsive materials architected in space and time. *Nat. Rev. Mater.* **7**, 683–701 (2022).
18. P. Jiao, J. Mueller, J. R. Raney, X. Zheng, A. H. Alavi, Mechanical metamaterials and beyond. *Nat. Commun.* **14**, 6004 (2023).
19. J. U. Surjadi, C. M. Portela, Enabling three-dimensional architected materials across length scales and timescales. *Nat. Mater.* **24**, 493–505 (2025).
20. C. Della Giovampaola, N. Engheta, Digital metamaterials. *Nat. Mater.* **13**, 1115–1121 (2014).
21. T. Chen, M. Pauly, P. M. Reis, A reprogrammable mechanical metamaterial with stable memory. *Nature* **589**, 386–390 (2021).
22. Z. Liu, M. Li, X. Dong, Z. Ren, W. Hu, M. Sitti, Creating three-dimensional magnetic functional microdevices via molding-integrated direct laser writing. *Nat. Commun.* **13**, 2016 (2022).
23. R. Poon, J. B. Hopkins, Phase-changing metamaterial capable of variable stiffness and shape morphing. *Adv. Eng. Mater.* **21**, 1900802 (2019).
24. J. K. Choe, J. Yi, H. Jang, H. Won, S. Lee, H. Lee, Y. Jang, H. Song, J. Kim, Digital mechanical metamaterial: Encoding mechanical information with graphical stiffness pattern for adaptive soft machines. *Adv. Mater.* **36**, e2304302 (2024).
25. B. Yang, R. Baines, D. Shah, S. Patiballa, E. Thomas, M. Venkadesan, R. Kramer-Bottiglio, Reprogrammable soft actuation and shape-shifting via tensile jamming. *Sci. Adv.* **7**, eabh2073 (2021).
26. Y. Wang, L. Li, D. Hofmann, J. E. Andrade, C. Daraio, Structured fabrics with tunable mechanical properties. *Nature* **596**, 238–243 (2021).
27. X. Fang, J. Wen, L. Cheng, D. Yu, H. Zhang, P. Gumbsch, Programmable gear-based mechanical metamaterials. *Nat. Mater.* **21**, 869–876 (2022).
28. C. Perez-Garcia, R. Zaera, J. Aranda-Ruiz, G. Bordiga, G. Risso, M. L. Lopez-Donaire, K. Bertoldi, D. Garcia-Gonzalez, Reprogrammable mechanical metamaterials via passive and active magnetic interactions. *Adv. Mater.* **37**, e2412353 (2025).
29. T. Zhao, X. Dang, K. Manos, S. Zang, J. Mandal, M. Chen, G. H. Paulino, Modular chiral origami metamaterials. *Nature* **640**, 931–940 (2025).
30. X. Hu, T. Tan, B. Wang, Z. Yan, A reprogrammable mechanical metamaterial with origami functional-group transformation and ring reconfiguration. *Nat. Commun.* **14**, 6709 (2023).

Downloaded from https://www.science.org on January 23, 2026

31. J. P. Udani, A. F. Arrieta, Programmable mechanical metastructures from locally bistable domes. *Extreme Mech. Lett.* **42**, 101081 (2021).
32. S. Li, B. Deng, A. Grinthal, A. Schneider-Yamamura, J. Kang, R. S. Martens, C. T. Zhang, J. Li, S. Yu, K. Bertoldi, J. Aizenberg, Liquid-induced topological transformations of cellular microstructures. *Nature* **592**, 386–391 (2021).
33. C. Li, F. Ellyin, A micro-macro correlation analysis for metal matrix composites undergoing multiaxial damage. *Int. J. Solids Struct.* **35**, 637–649 (1998).
34. A. B. M. T. Haque, D. H. Ho, D. Hwang, R. Tutika, C. Lee, M. D. Bartlett, Electrically conductive liquid metal composite adhesives for reversible bonding of soft electronics. *Adv. Funct. Mater.* **34**, 2304101 (2024).
35. G. Lee, E. Ray, H.-J. Yoon, S. Genovese, Y. S. Choi, M.-K. Lee, S. Şahin, Y. Yan, H.-Y. Ahn, A. J. Bandodkar, J. Kim, M. Park, H. Ryu, S. S. Kwak, Y. H. Jung, A. Odabas, U. Khandpur, W. Z. Ray, M. R. MacEwan, J. A. Rogers, A bioresorbable peripheral nerve stimulator for electronic pain block. *Sci. Adv.* **8**, eabp9169 (2022).
36. B. Lee, H. Cho, K. T. Park, J.-S. Kim, M. Park, H. Kim, Y. Hong, S. Chung, High-performance compliant thermoelectric generators with magnetically self-assembled soft heat conductors for self-powered wearable electronics. *Nat. Commun.* **11**, 5948 (2020).
37. R. W. Style, R. Tutika, J. Y. Kim, M. D. Bartlett, Solid-liquid composites for soft multifunctional materials. *Adv. Funct. Mater.* **31**, 2005804 (2021).
38. R. W. Style, R. Boltyanskiy, B. Allen, K. E. Jensen, H. P. Foote, J. S. Wettlaufer, E. R. Dufresne, Stiffening solids with liquid inclusions. *Nat. Phys.* **11**, 82–87 (2015).
39. C. Zeni, R. Pinsler, D. Zügner, A. Fowler, M. Horton, X. Fu, Z. Wang, A. Shysheya, J. Crabbé, S. Ueda, R. Sordillo, L. Sun, J. Smith, B. Nguyen, H. Schulz, S. Lewis, C.-W. Huang, Z. Lu, Y. Zhou, H. Yang, H. Hao, J. Li, C. Yang, W. Li, R. Tomioka, T. Xie, A generative model for inorganic materials design. *Nature* **639**, 624–632 (2025).
40. N. Kim, D. Lee, C. Kim, D. Lee, Y. Hong, Simple arithmetic operation in latent space can generate a novel three-dimensional graph metamaterials. *npj Comput. Mater.* **10**, 236 (2024).
41. R. L. Truby, Designing soft robots as robotic materials. *Acc. Mater. Res.* **2**, 854–857 (2021).
42. M. R. Devlin, S. Kim, O. Campàs, E. W. Hawkes, Material-like robotic collectives with spatiotemporal control of strength and shape. *Science* **387**, 880–885 (2025).
43. H. Cui, D. Yao, R. Hensleigh, H. Lu, A. Calderon, Z. Xu, S. Davaria, Z. Wang, P. Mercier, P. Tarazaga, X. Zheng, Design and printing of proprioceptive three-dimensional architected robotic metamaterials. *Science* **376**, 1287–1293 (2022).
44. R. H. Lee, E. A. B. Mulder, J. B. Hopkins, Mechanical neural networks: Architected materials that learn behaviors. *Sci. Robot.* **7**, eabq7278 (2022).
45. H. Yasuda, P. R. Buskohl, A. Gillman, T. D. Murphey, S. Stepney, R. A. Vaia, J. R. Raney, Mechanical computing. *Nature* **598**, 39–48 (2021).
46. Y. Zhang, C. Fowler, J. Liang, B. Azhar, M. Y. Shalaginov, S. Deckoff-Jones, S. An, J. B. Chou, C. M. Roberts, V. Liberman, M. Kang, C. Ríos, K. A. Richardson, C. Rivero-Baleine, T. Gu, H. Zhang, J. Hu, Electrically reconfigurable non-volatile metasurface using low-loss optical phase-change material. *Nat. Nanotechnol.* **16**, 661–666 (2021).
47. S. Abdollahramezani, O. Hemmatyar, M. Taghinejad, H. Taghinejad, A. Krasnok, A. A. Eftekhar, C. Teichrib, S. Deshmukh, M. A. El-Sayed, E. Pop, M. Wuttig, A. Alù, W. Cai, A. Adibi, Electrically driven reprogrammable phase-change metasurface reaching 80% efficiency. *Nat. Commun.* **13**, 1696 (2022).
48. A. C. Karacakol, Y. Alapan, S. O. Demir, M. Sitti, Data-driven design of shape-programmable magnetic soft materials. *Nat. Commun.* **16**, 2946 (2025).
49. H. Deng, K. Sattari, Y. Xie, P. Liao, Z. Yan, J. Lin, Laser reprogramming magnetic anisotropy in soft composites for reconfigurable 3D shaping. *Nat. Commun.* **11**, 6325 (2020).
50. H. Wang, S. Chen, H. Li, X. Chen, J. Cheng, Y. Shao, C. Zhang, J. Zhang, L. Fan, H. Chang, R. Guo, X. Wang, N. Li, L. Hu, Y. Wei, J. Liu, A liquid gripper based on phase transitional metallic ferrofluid. *Adv. Funct. Mater.* **31**, 2100274 (2021).
51. X. Wang, X. Lu, W. Xiao, X. Liu, L. Li, H. Chang, Z. Yu, X. Yang, L. Chang, K. Sun, Q. Wang, C. Jiao, L. Hu, Fast solidification of pure gallium at room temperature and its micromechanical properties. *Adv. Mater. Interfaces* **10**, 2202100 (2023).
52. R. Li, L. Li, T. Yu, L. Wang, J. Chen, Y. Wang, Z. Cai, J. Chen, M. L. Rivers, H. Liu, Study of liquid gallium as a function of pressure and temperature using synchrotron x-ray microtomography and x-ray diffraction. *Appl. Phys. Lett.* **105**, 041906 (2014).
53. I. D. Joshipura, C. K. Nguyen, C. Quinn, J. Yang, D. H. Morales, E. Santiso, T. Daeneke, V. K. Truong, M. D. Dickey, An atomically smooth container: Can the native oxide promote supercooling of liquid gallium? *iScience* **26**, 106493 (2023).
54. H. Niu, L. Bonati, P. M. Piaggi, M. Parrinello, Ab initio phase diagram and nucleation of gallium. *Nat. Commun.* **11**, 2654 (2020).
55. Z. Xia, Y. Zhang, F. Ellyin, A unified periodical boundary conditions for representative volume elements of composites and applications. *Int. J. Solids Struct.* **40**, 1907–1921 (2003).
56. A. Mueller, M. C. Wapler, U. Wallrabe, A quick and accurate method to determine the poisson's ratio and the coefficient of thermal expansion of pdms. *Soft Matter* **15**, 779–784 (2019).
57. Y. Xue, D. Kang, Y. Ma, X. Feng, J. A. Rogers, Y. Huang, Collapse of microfluidic channels/reservoirs in thin, soft epidermal devices. *Extreme Mech. Lett.* **11**, 18–23 (2017).
58. B. Liu, Y. Huang, H. Jiang, S. Qu, K. Hwang, The atomic-scale finite element method. *Comput. Methods Appl. Mech. Eng.* **193**, 1849–1864 (2004).
59. H. Laubie, S. Monfared, F. Radjaï, R. Pellenq, F.-J. Ulm, Disorder-induced stiffness degradation of highly disordered porous materials. *J. Mech. Phys. Solids* **106**, 207–228 (2017).
60. K. McGarigal, B. J. Marks, *FRAGSTATS: Spatial Pattern Analysis Program for Quantifying Landscape Structure* (US Department of Agriculture, Forest Service, Pacific Northwest Research Station, 1995).
61. M. J. Mirzaali, H. Pahlavani, A. A. Zadpoor, Auxeticity and stiffness of random networks: Lessons for the rational design of 3D printed mechanical metamaterials. *Appl. Phys. Lett.* **115**, 021901 (2019).
62. C. Wang, H. Zhao, Spatial heterogeneity analysis: Introducing a new form of spatial entropy. *Entropy* **20**, 398 (2018).
63. G. Kafkopoulos, C. J. Padberg, J. Duvigneau, G. J. Vancso, Adhesion engineering in polymer-metal comolded joints with biomimetic polydopamine. *ACS Appl. Mater. Interfaces.* **13**, 19244–19253 (2021).
64. A. Frick, M. Rettenberger, M. Spadaro, Evaluation of the interfacial adhesion between polymer and metal on polymer-metal hybrids. *Polym. Test.* **106**, 107448 (2022).
65. J. Bowling, G. W. Groves, The debonding and pull-out of ductile wires from a brittle matrix. *J. Mater. Sci.* **14**, 431–442 (1979).
66. C. Wang, Fracture mechanics of single-fibre pull-out test. *J. Mater. Sci.* **32**, 483–490 (1997).
67. S. H. Jeong, Z. Shou, K. Hjort, J. Hilborn, Z. Wu, Pdms-based elastomer tuned soft, stretchable, and sticky for epidermal electronics. *Adv. Mater.* **28**, 5830–5836 (2016).

Acknowledgments: This work was performed in part at the Duke University Shared Materials Instrumentation Facility, a member of the North Carolina Research Triangle Nanotechnology Network, which is supported by the National Science Foundation (award no. ECCS-2025064) as part of the National Nanotechnology Coordinated Infrastructure. X.N. thanks M. D. Dickey, M. Han, D. Zhuo, and J. Yin for helpful discussions. **Funding:** Y.B., Y.W., and X.N. acknowledge funding support from the Beyond the Horizon Initiative of the Pratt School of Engineering at Duke University. **Author contributions:** Y.B., H.W., and X.N. conceived the idea and designed the research. Y.B. and Y.W. fabricated the samples. Y.B., Y.W., and K.Y. performed the experiments. X.Y. and H.W. performed the FE modeling and theoretical study. Y.B. and X.N. analyzed the experimental data. Y.B., X.Y., H.W., and X.N. wrote the manuscript, with input from all coauthors. **Competing interests:** X.N. and Y.B. are listed as coinventors on a patent application (US application no. 63/813,785) that covers the design, fabrication, and application of the digital solid-liquid composite. The other authors declare that they have no competing interests. **Data and materials availability:** All data and code needed to evaluate and reproduce the results in the paper are present in the paper and/or the Supplementary Materials. Source data underlying the figures and the analysis code used in this study are publicly available on Figshare with the identifier https://doi.org/10.6084/m9.figshare.29362844. For detailed instructions and documentation, please refer to the GitHub repository at https://github.com/ni-x-lab/PM.

Submitted 19 November 2025
Accepted 24 December 2025
Published 23 January 2026
10.1126/sciadv.aed9698

Downloaded from https://www.science.org on January 23, 2026